Experimental Verification of Ir 5d Orbital States and Atomic Structures in Highly Active Amorphous Iridium Oxide Catalysts

Gihan Kwon,* Seo Hyoung Chang,* Jin Eun Heo, Kyeong Jun Lee, Jin-Kwang Kim, Byeong-Gwan Cho, Tae Yeong Koo, B. J. Kim, Chanseok Kim, Jun Hee Lee, Seong-Min Bak, Kevin A. Beyer, Hui Zhong, Robert J. Koch, Sooyeon Hwang, Lisa M. Utschig, Xiaojing Huang, Gongfang Hu, Gary W. Brudvig, David M. Tiede, and Jungho Kim*

ACCESS | Metrics & More | Article Recommendations | Supporting Information

ABSTRACT: In iridium oxide catalysts, the electronic states whose energies are in the range of energetics and charge transfer kinetics of the oxygen evolution reaction (OER) originate from the Ir 5d orbital states. However, the understanding of the atomic structures and orbital states underlying catalytic reactivity in amorphous iridium oxide oxygen evolving catalysts (Ir-OECs) is incomplete compared to that of crystalline oxides, owing to a lack of direct experimental verification. Here, we present experimental approaches using resonant inelastic X-ray scattering (RIXS) to directly access Ir 5d orbital excitations at the Ir L_3 edge and atomic pair distribution function (PDF) measurements to characterize electronic and coordination structures at the atomic scale. The so-called iridium blue layer (IrBL) and IrO_x were formed from the organometallic precursor complex $[Cp*Ir(H_2O)_3]SO_4$ and the inorganic precursor $IrCl_3$, respectively. *Ex situ* IrBL and IrO_x films for RIXS and PDF measurements were prepared by conditioning electrodeposited films at a low voltage. The incident energy RIXS profile of IrO_x exhibited extra weak resonantly enhanced excitation below 2 eV energy loss. The feature was clearly different from a single high-energy excitation above 3 eV of IrBL related to the interband transition between π- and σ-antibonding states. The atomic structure refinement based on PDF measurements revealed the atomic structure domains to have edge- and corner-shared IrO_6 octahedra with trigonal-type distortion. Density functional theory calculations guided by the refined atomic structures shed light on the electronic structure corresponding to experimental results, including insulating and metallic phases in *ex situ* IrBL and IrO_x films, respectively. Our study establishes different Ir 5d orbital states and atomic structures in two amorphous Ir oxide OER catalysts in their reduction states.

KEYWORDS: iridium oxide, iridium blue layer, water oxidation, water splitting, resonant inelastic X-ray scattering (RIXS), pair distribution function (PDF)
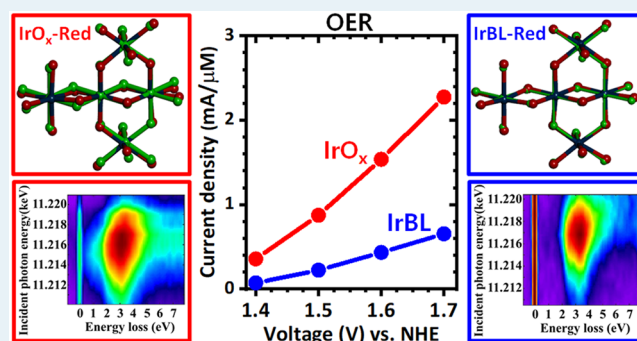
INTRODUCTION

Hydrogen is an alternative energy storage and fuel source, which is sustainable and eco-friendly. Water electrolysis is a promising process for hydrogen production, but its sluggish kinetics, severe corrosion of catalysts in harsh acidic conditions, and reduction of noble metal usage still remain a challenge.[1−6] It has been shown that iridium oxide oxygen evolving catalysts (Ir-OECs) show high oxygen evolution reaction (OER) activity and sufficient stability in acidic conditions.[7−10] Several recent results have demonstrated that Ir-OECs with amorphous structures exhibit higher OER activities than those of crystalline Ir-OECs.[9,11−15] Ir-OECs have been investigated by cyclic voltammogram (CV), density functional theory (DFT) calculation,[16] X-ray absorption near-edge spectroscopy (XANES),[8,17−25] and X-ray photoelectron

spectroscopy (XPS),[26] in multimodal approaches.[3,5,14,15] Despite extensive effort, information on how atomic-level structure and electronic structures of amorphous Ir-OECs contribute to OER catalytic performance remains largely obscure.

Experimental verification on the electronic structure of the Ir-OEC requires taking into account the fact that 5d systems have fundamentally different electronic structures from 3d
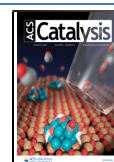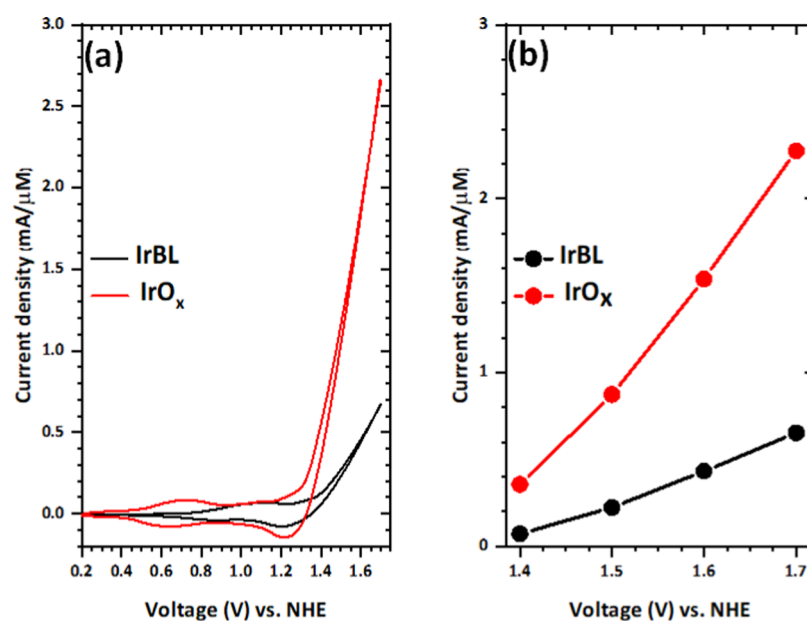
Figure 1. (a) Cyclic voltammogram (CV) and (b) steady-state current density of IrBL and IrO_x as a function of voltage. Film thicknesses of IrBL and IrO_x are about 600 and 500 nm shown in Table S1. Thickness-dependent CV and steady-state current density are shown in Figure S4 and Table S2.

systems because the 5d orbitals are spatially more extended than the 3d orbitals. In the 3d systems, the density of states near the Fermi level is a complex mixture of 3d and ligand states. The Coulomb repulsion between neighboring 3d ions and the charge transfer energy between ligand and 3d ion play key roles in electronic states relevant for the OER.[27] On the other hand, in the 5d systems, the large atomic number (Z) and the spatially extended nature of the 5d orbital lead to a stronger ligand—metal hybridization, a larger bandwidth, and a larger crystal-field splitting. Ligand bonding states are located at much lower energies from the Fermi level, while the charge transfer excitations from ligand to Ir 5d states are located at much higher energy than the energy required for the OER operation. Hence, 5d orbital states in the 5d systems dictate physical and chemical properties.

The structural environment of Ir and its local coordinate can govern the electronic structure and OER catalysis performance. 5d orbital states are split into sublevels due to the ligand crystal field. In the octahedral symmetry, for example, the density of states near the Fermi level consists only of the t_{2g} (π-symmetry antibonding) states, while the e_g (σ-symmetry antibonding) states are located above the Fermi level due to larger crystal-field splitting. The large t_{2g} bandwidth with a weaker on-site Coulomb repulsion often results in metallic ground states or small gap insulating states due to the strong spin—orbit coupling.[28] So, electronic states relevant for the OER are formed within Ir 5d orbital states. Oxygen orbitals are involved in the formation of the crystal field, and hybridization and oxygen vacancy can affect the Ir valency and subsequently the electronic structure. In amorphous iridium oxides, however, it is not a priori clear that this picture from a crystalline system is valid for a < 1 nm domain structure which contains defects, distortions, and diverse short-ranged ordered structure.[15,29,30] Hence, it is crucial to verify both 5d orbital electronic state and atomic structure of amorphous iridium oxide catalyst for solving the hidden energetics, which were closely related to charge transfer kinetics of its OER.

In this work, we study two amorphous iridium oxide oxygen evolving catalysts (Ir-OECs): the so-called iridium blue layer (IrBL)[9,10,29,31] from the organometallic precursor complex $[Cp*Ir(H_2O)_3]SO_4$ and IrO_x from the inorganic precursor $IrCl_3 \cdot H_2O$. We present measurements of resonant inelastic X-ray scattering (RIXS) at the Ir L_3 edge and atomic pair distribution function (PDF) on *ex situ* IrBL and IrO_x samples, which were prepared in the form of dried films after conditioned for 1 h at 0.5 V vs normal hydrogen electrode (NHE) (reduction condition) in pH 2.85 of 0.1 M KNO_3 electrolyte solutions. IrBL-Red and IrO_x-Red will refer to these *ex situ* samples in the rest of the paper. At the Ir L_3 edge, dipole transition gives rise to the direct RIXS via 2p → 5d absorption and subsequent 5d → 2p decay, which directly probes the valence and conduction of the 5d states.[32] The PDF data of IrBL-Red and IrO_x-Red are reasonably described by an atomic structure of edge- and corner-shared IrO_6 octahedra with longer Ir—O bond lengths and smaller edge- and larger corner-sharing bond angles than the rutile IrO_2. Band structure calculations have been carried out based on the refined atomic structures in IrBL-Red and IrO_x-Red. Our study of RIXS, PDF, and band structure calculations establishes that highly active amorphous Ir oxide OER catalysts share the basic electronic structure aspect of the octahedra-based crystalline Ir oxide but accommodate different Ir 5d orbital states and structural distortions in their reduction states.

◼ RESULTS

Growth Characteristic and Oxygen Evolution Performance of Amorphous Ir-OECs. IrBL films were electrolytically deposited on fluorine-doped tin oxide (FTO) substrate at 1.4 V vs normal hydrogen electrode (NHE) in potassium nitrate (KNO_3) electrolyte solution containing $[Cp*Ir(H_2O)_3]SO_4$ (Cp* = pentamethylcyclopentadienyl). The patented $[Cp*Ir(H_2O)_3]SO_4$ precursor results in a fast film growth.[9,10,29,31] The KNO_3 electrolyte solution containing chloride hydrate ($IrCl_3 \cdot H_2O$) was used to prepare IrO_x films

on FTO substrate at 1.4 V vs NHE. The precursor dissolution and the film growth rate are much slower in IrO_x compared to IrBL. (Further experimental information is provided in Figure S1 and Table S1.)

Figure 1 compares IrBL and IrO_x films deposited for 150 and 1000 min, which were used for the PDF and RIXS measurements. The thicknesses of those films were estimated to be ∼600 and 500 nm, respectively, by the scanning electron microscope (SEM) (see Figure S1), indicating the similar geometrical dimensions of those films. The Ir contents in IrBL and IrO_x were measured in the unit of micromolar concentration (μM) by the inductively coupled plasma (ICP) analysis (details in the Experimental Procedures section in the Supporting Information.) Figure 1a shows cyclic voltammogram (CV) data of IrBL and IrO_x, which were collected in pH 2.85 of 0.1 M KNO_3 and normalized by the Ir contents.

In both films, pre-features are seen in the low-voltage region before the onset of the oxide formation (>1.23 V). These pre-features can be explained by the quasi-reversible internal redox event of the surface-bound layer or adsorption of hydroxyl species.[8,10,12] In the case of the IrBL, the oxidation wave peak in the anodic sweep is centered at 1.1 V, but the reduction wave peak in the cathodic sweep is centered at 0.9 V. The large voltage difference between the two peaks indicates that the IrBL has a large overpotential. Figure S4a shows that the overpotential is smaller in the case of thin 100 nm thickness IrBL film (30 min growth time). Even though we cannot rule out the possible effects of different surface functional groups, we attribute the large overpotential in the thicker IrBL to poor electric conductivity. On the other hand, the pre-features of IrO_x are seen at a similar lower voltage of 0.7 V, indicating that IrO_x has a different kinetic.[8,10] As shown in Figure S4b, IrO_x films with all of the thicknesses showed similar small overpotentials, indicating that IrO_x has good electric conductivity. As correlated with the higher overpotential, IrBL showed a lower OER activity than IrO_x. Figure 1b shows the steady-state current density of IrBL and IrO_x in the unit of mA/μM as a function of applied potentials. The IrBL film shows the OER activity of about 0.65 mA/uM at 1.7 V. On the other hand, the IrO_x film shows a much higher OER activity of 2.27 mA/μM at 1.7 V.

PDFs and Structural Refinements of IrBL-Red and IrO_x-Red. In Figure 2, the PDF patterns of IrBL-Red and IrO_x-Red are presented and compared with those of two other amorphous Ir-OECs prepared by different synthetic methods[29,30] and the crystalline rutile IrO_2.[20,30] The BL[29] was identical with the IrBL-Red in this study regarding the precursor complex but different from the IrBL-Red in this study because it was deposited on indium tin oxide glass electrode in 0.1 M KNO_3 with the iridium precursor and was not post-conditioned in 0.1 M KNO_3 (pH 2.85) unlike the IrBL-Red. IrO_x-FHI represents the IrO_x synthesized at the Department of Inorganic Chemistry of the Fritz Haber Institute.[30] The rutile IrO_2 is the commercial powder from Alfa-Aesar.[30] The PDF pattern of the crystalline rutile IrO_2 is well understood.[30] The first peak around 2 Å is assigned to the Ir–O bond distance, and the second and third peaks are assigned to the Ir–Ir atomic pair distances of edge-sharing and corner-sharing octahedra, respectively. It is seen in Figure 2 that the PDF patterns of all four amorphous Ir-OECs are characterized by these three prominent peak structures, indicating that all four amorphous Ir-OECs share the similar
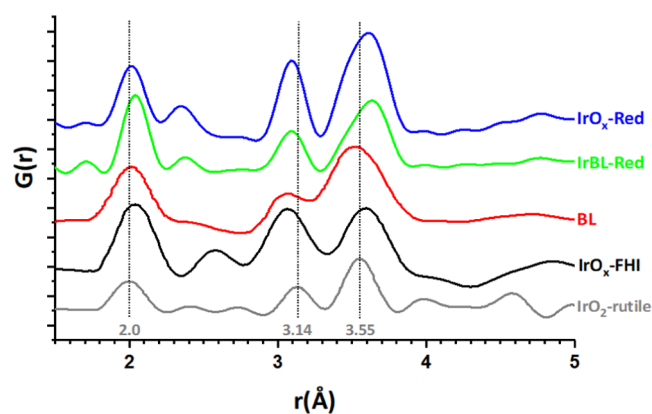

Figure 2. Comparisons of pair distribution function (PDF) patterns between IrO_2-rutile and several OECs (IrO_x-FHI, BL, IrBL-Red, IrO_x-Red). The PDF patterns, denoted by G(r), of BL, IrO_2-rutile, and IrO_x-FHI, were digitized from refs 29, 30. The dot lines indicate peak positions of IrO_2-rutile. See Figures S5 and S6 for the color change of Ir-OECs and the whole range of PDF data in the Supporting Information, respectively.

core structure of linked edge- and corner-shared IrO_6 octahedra. In all four amorphous Ir-OECs, the first peak is slightly above 2 Å, indicating that the Ir–O bond lengths are larger than 2 Å. The second peak is shorter than that in the IrO_2 reference structure (3.14 Å), indicating a shorter Ir–Ir atom pair distance between iridium atoms connected by di-μ-oxo bonding in the amorphous materials. The third peak is shifted to longer distances than that in IrO_2 (3.55 Å) except the BL, indicating longer Ir–Ir atom pair distances between iridium atoms connected by mono-μ-oxo bonding.

To simulate the PDF spectra of IrBL-Red and IrO_x-Red, we started with the atomic structure model[29] that was constructed by extracting Ir-oxo fragments from the rutile IrO_2 structure. Both IrBL-Red and IrO_x-Red spectra in Figure 3a,b, respectively, consist of the well-resolved correlation peaks up to about 8 Å, which is similar in the BL.[29] This mother model comprises three edge-sharing and two corner-sharing octahedra, as shown in Figure 3a,b (green spheres and rods). In Figure 3a,b, it is noted that the amplitude of the first Ir–O bond peak is higher in IrBL-Red than in IrO_x-Red, while the amplitude of the second edge-sharing Ir–Ir peak is higher in IrO_x-Red than in IrBL-Red. A small percentage of octahedral fragments was assumed to describe such a large amplitude difference. A fraction (5.5% shown in Figure S11) of single octahedrons was used for the IrBL-Red, while a fraction (10% shown in Figure S12) of three edge-sharing octahedra was used for the IrO_x-Red. The final pair distribution functions in Figure 3a,b were derived by linearly combining all contributions. A detailed description of the PDF pattern fit is provided in Figures S7–S12 and Tables S3–S6 and elsewhere.[33] The residual or goodness of fit residual, R_w, is 0.32 and 0.26 for IrBL-Red and IrO_x-Red, respectively.

In the rutile IrO_2, the site symmetry of Ir is D_{2h}, where the e_g level is split into the a_{1g} and b_{1g} levels (σ-symmetry) and the t_{2g} level is split into the e_g and b_{2g} levels (π-symmetry). The band structure calculations[34] found that the σ-symmetry antibonding states form well-defined conduction states well above the Fermi level even with the D_{2h} crystal-field splitting because of the large crystal-field. The π-symmetry antibonding states form valence states which have bandwidths as large as 10 eV and so is marginally affected by the D_{2h} crystal-field splitting. The π-
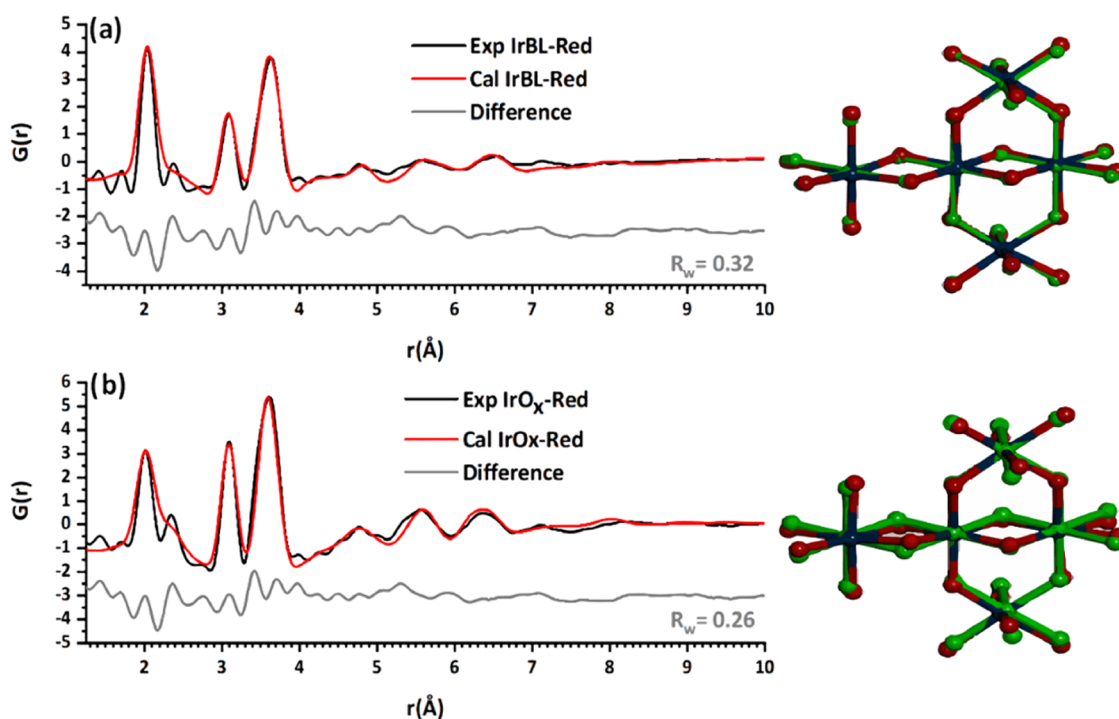
Figure 3. Refined PDF patterns of IrBL-Red and IrO$_x$-Red. Comparison of the experimental and calculated G(r) spectra for (a) IrBL-Red and (b) IrO$_x$-Red.

symmetry antibonding state is solely responsible for the density of states near the Fermi level and the metallic carriers.

Figure 3a,b shows the derived atomic structures (red spheres and blue rods) of IrBL-Red and IrO$_x$-Red, respectively, derived from the PDF refinements with the mother model (green spheres and rods) from the rutile IrO$_2$. The atom pair distances and angles in IrBL-Red and IrO$_x$-Red are noticeably different from the mother model from the rutile IrO$_2$, as summarized in Table 1. With the longer Ir−O bond lengths, the bond angles

Table 1. Average Lengths and Angles of IrBL-Red and IrO$_x$-Red Derived from the PDF in Figure 3 [a]

	length (Å)			angle (deg)	
OECs	Ir−O	Ir−Ir (edge)	Ir−Ir (corner)	α	β
IrBL-Red	2.041	3.089	3.634	98.35	125.81
IrO$_x$-Red	2.017	3.100	3.610	100.43	126.99
IrO$_2$	2.000	3.140	3.550	103.44	125.12

[a] α and β indicate angles in the edge- and corner-sharing, respectively, Ir−Ir bonds.

of the edge-sharing (α) octahedra in IrBL-Red and IrO$_x$-Red are closer to 90° than that in the rutile IrO$_2$, indicating that the tetragonal distortion which leads to the D$_{2h}$ site symmetry of Ir is lesser in IrBL-Red and IrO$_x$-Red compared to the rutile IrO$_2$. On the other hand, the bond angles of the corner-sharing (β) octahedra in IrBL-Red and IrO$_x$-Red are slightly larger than that in the rutile IrO$_2$. The structures of IrBL-Red and IrO$_x$-Red also show a type of trigonal distortion, which is found in Ti$_2$O$_3$,[34] which is larger in IrO$_x$-Red than in IrBL-Red, as seen in Figure S13 and the insets of Figure 3.

Here, the site symmetry of Ir is C$_{3i}$, where the t$_{2g}$ level is split into the e$_g$ and a$_{2g}$ levels but the e$_g$ level keeps its symmetry level. Regarding the electronic structure, longer Ir−O bond lengths and smaller edge-sharing angles in IrBL-Red and IrO$_x$-Red are expected to lead to a smaller bandwidth and a smaller crystal-field splitting between π- and σ-symmetry states. Whether the electronic structures of IrBL-Red and IrO$_x$-Red share characteristics of the Ir 5d orbital structure in the crystalline IrO$_2$ is an outstanding question that can be answered by the RIXS measurements at the Ir L$_3$ edge.

Electronic Structure and RIXS Spectrum of Iridium Oxide. As an introduction, the schematic descriptions of the Ir 5d orbital states, the RIXS processes, and the resulting RIXS spectra are shown in Figure 4. Figure 4a shows the band diagram of iridium oxides consisting of IrO$_6$ octahedra. Antibonding Ir 5d orbitals t$_{2g}$ (π-symmetry) and e$_g$ (σ-symmetry) comprise the density of states around the Fermi level. Bonding oxygen states are located below the t$_{2g}$ states and are not indicated. "10Dq" denotes average energy separation (or crystal-field splitting) between e$_g$ and t$_{2g}$. The extended nature of 5d orbitals leads to a large crystal-field splitting and typically 10Dq is in the range of 3−4 eV. In the Ir(IV) oxidation state, there are five electrons to fill the Ir 5d orbitals, and so there is one hole in the t$_{2g}$, leading to a metallic ground state.[35,36] In solids, the strong spin−orbit coupling further splits t$_{2g}$ orbitals into a narrow band state and a small gap insulating state can be realized with a weaker Coulomb repulsion of 5d orbital.[28] In the Ir(III) oxidation state, six electrons fully fill the t$_{2g}$ orbitals, leading to an insulating ground state.

Figure 4b shows the RIXS process. The incident X-ray (E_i) is tuned to promote 2p$^{3/2}$ core electrons to either unoccupied e$_g$ or t$_{2g}$ states. Subsequently, the occupied t$_{2g}$ electrons fill the 2p$^{3/2}$ core hole, leaving excitations between occupied and unoccupied 5d orbitals. Figure 4c shows the resulting RIXS spectra of Ir(IV) and Ir(III) cases. Partially unoccupied antibonding t$_{2g}$ in Ir(IV) gives rise to a low-energy scattering intensity filling the low energy loss region, which extends to the zero energy loss. The higher-energy loss feature originates from
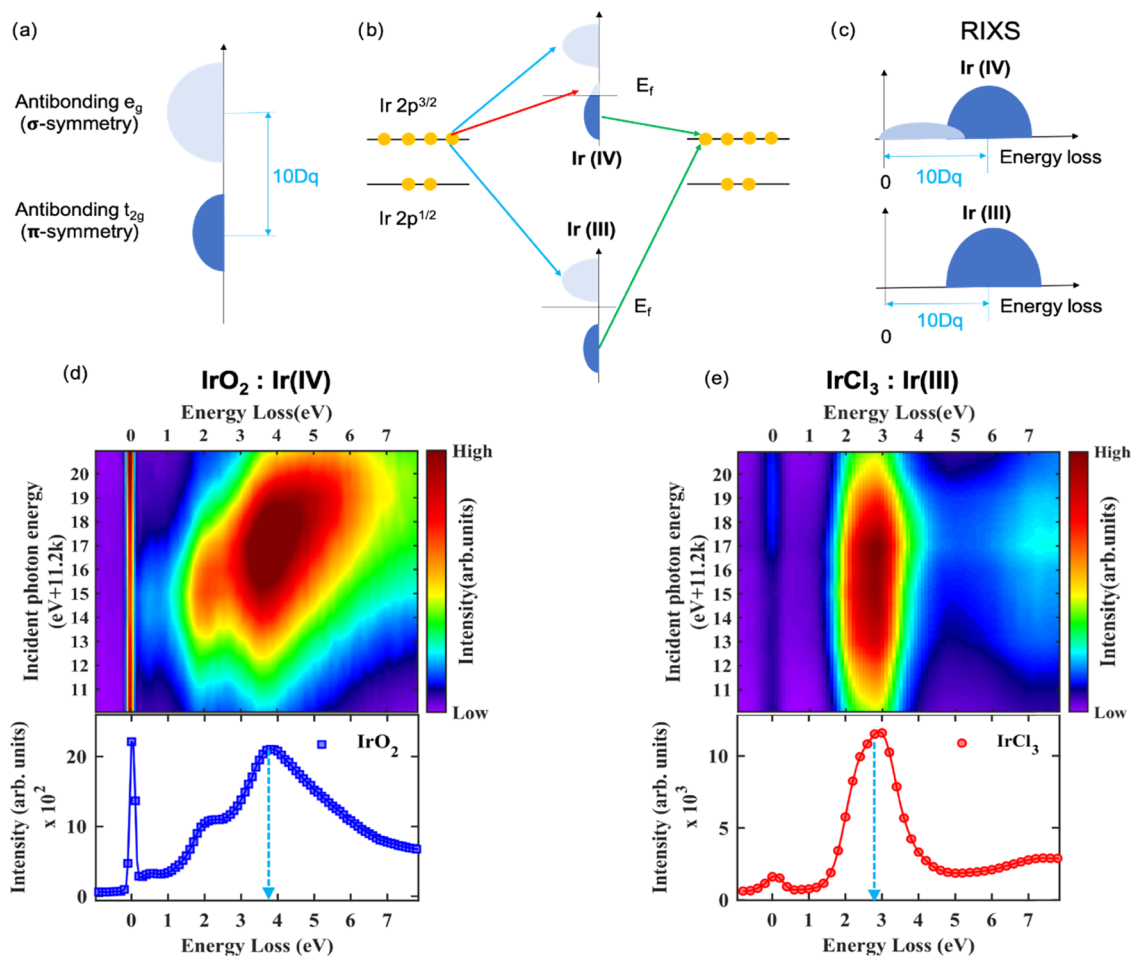
Figure 4. Electronic structures and excitation spectra of iridium oxides. (a) Schematic band diagram of iridium oxides consisting of IrO_6 octahedra. (b, c) Schematic diagrams for direct Ir L_3 RIXS processes and spectra, respectively, in cases of Ir(IV) and Ir(III). The excitation between unoccupied e_g and occupied t_{2g} state gives rise to a higher-energy loss feature whose amplitude is peaked at 10Dq. Partially unoccupied t_{2g} in Ir(IV) gives rise to a scattering intensity at low energy loss, which is absent for the case of Ir(III). (d, e) RIXS spectra vs E_i for reference samples Ir(IV)O_2 and Ir(III)Cl_3, respectively. Energy loss spectra summed over all measured E_i are shown in the bottom panels.

transitions between antibonding e_g and t_{2g}, representing the 10Dq. The onset energy of the higher-energy peak reflects the onset energy of the unoccupied antibonding e_g state because the Fermi level crosses the antibonding t_{2g} states. In the Ir(III) case, unlike the Ir(IV) case, there is no low-energy scattering intensity below the onset energy. The identification of the Ir(III) is direct and definitive in the Ir L_3 edge RIXS spectrum of the octahedral Ir oxide.

To illustrate the details mentioned above, two samples, rutile IrO_2 and $IrCl_3$ were measured as reference samples of Ir(IV) and Ir(III), respectively. Figure 4d shows the image plot of the full incident energy (E_i) dependence spectra of IrO_2. The scattering intensity at the zero energy loss is the elastic scattering. At around E_i = 11.215 keV, two low-energy peaks around 0.5 and 2 eV are seen to resonate. At around E_i = 11.217 keV, the high-energy peak around 4 eV is seen to become resonantly strong.

The first two peaks are assigned to the excitation within the π-symmetry (t_{2g}-like) manifolds (between one unoccupied hole and five occupied electrons). The high-energy peak (3.8 eV) is assigned to the excitation between unoccupied σ-antibonding (e_g-like) and occupied π-antibonding (t_{2g}-like) state. The higher E_i is easily understood because of the higher energy of the $2p^{3/2} \rightarrow \sigma$ state absorption than the $2p^{3/2} \rightarrow \pi$

state. Figure 4e shows the image plot of the full E_i dependence spectra of $IrCl_3$. For all measured E_i, there is no low-energy scattering intensity below 1.5 eV, and only one peak around 2.7 eV is seen. Clearly, this high-energy peak is assigned to the excitation between unoccupied σ-antibonding and occupied π-antibonding state and the 10Dq is estimated to be about 2.7 eV.

RIXS spectra provide detailed information on the electronic structure of iridium oxide and clearly reflect differences in IrO_2 and $IrCl_3$ electronic structures. The 10Dq is higher in IrO_2 than in $IrCl_3$, reflecting a stronger ligand field in IrO_2. The excitation width is much broader in IrO_2 than in $IrCl_3$, reflecting a larger 5d bandwidth in IrO_2. The clearest difference is in the low-energy spectral weight. From the $IrCl_3$ Ir(III) spectra, we learn that the Ir(III) identification is definitive when there is no low-energy spectral weight for all incident energies. Therefore, the incident energy dependence RIXS measurement of iridium oxide is an effective way to distinguish excitations between antibonding σ and π states and know the 5d orbital state of the Ir ion.

RIXS Spectra of IrBL-Red and IrO$_x$-Red. IrBL-Red and IrO$_x$-Red films were prepared just before the measurement and placed in the flowing He gas during the RIXS measurement[37,38] to minimize possible degradation or oxidation in the
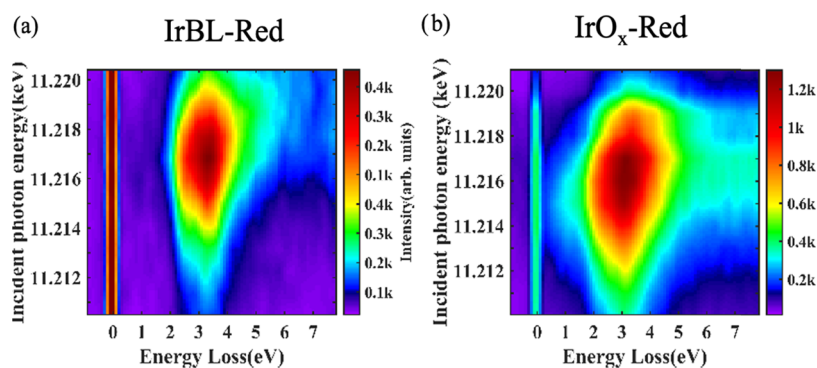
Figure 5. RIXS spectra vs E_i of IrBL-Red and IrO$_x$-Red. (a) IrBL-Red: The maximum intensity is located around 3.4 eV. There is no clear intensity below 2 eV, indicating a nearly filled π-antibonding state of the Ir(III) oxidation state. (b) IrO$_x$-Red: The maximum intensity is located around 3.2 eV. The low energy loss region below 2 eV shows a finite scattering intensity, indicating a partially filled π-antibonding state.
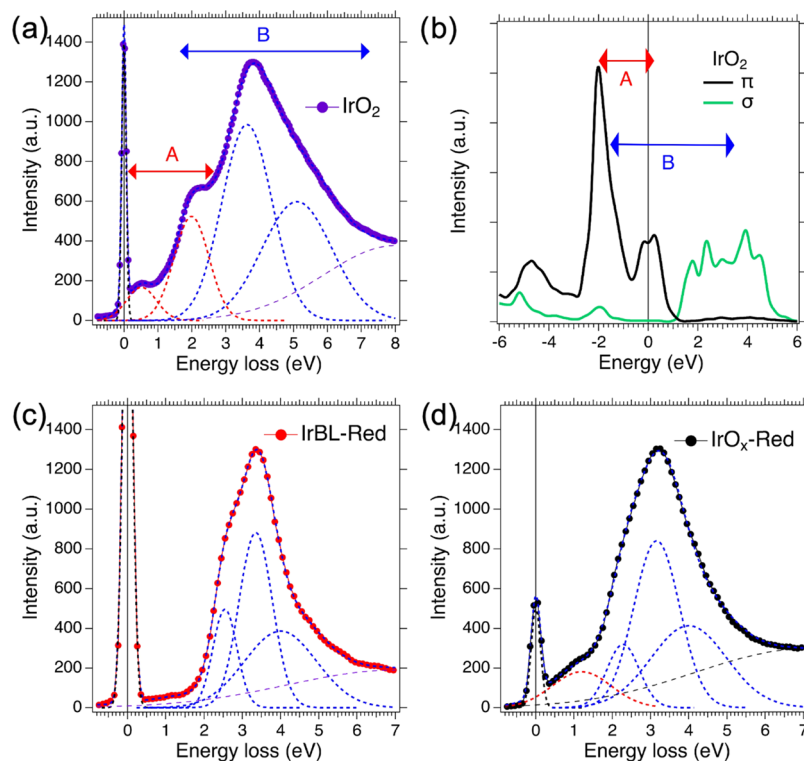

Figure 6. Integrated RIXS spectra were obtained by summing over all measured E_i dependence spectra. (a) IrO$_2$. The low-energy region below 3 eV (indicated by A) is fitted with two peaks at around 0.5 and 2 eV, and the high-energy region above 3 eV (indicated by B) is fitted with two peaks at around 3.7 and 5.3 eV. (b) Density functional theory calculations of the 5d orbitals for IrO$_2$. The excitations in the A region originate from excitations within the π states. The transitions from π to σ states contribute to the B region excitations. The high-energy excitations in (c) IrBL-Red and (d) IrO$_x$-Red are fitted with three Gaussian functions. One broad Gaussian function is added to describe the broad low-energy excitation in IrO$_x$-Red.

air. Preliminarily, we have carried out the X-ray photon flux study on IrBL-Red and IrO$_x$-Red. While the RIXS spectrum of IrO$_x$-Red was identical irrespective of high and low X-ray flux, the RIXS spectrum of IrBL-Red showed X-ray-induced irreversible change upon high X-ray flux (see Figures S14 and S15). A low X-ray flux that does not cause irreversible change was used for the measurement.

Figure 5a presents the full E_i dependence spectra of IrBL-Red. It is clearly seen that there is no intensity below 2 eV and only a single feature around 3.3 eV whose intensity is resonantly peaked at around E_i = 11.217 keV. These RIXS spectra of IrBL-Red resemble those of the Ir(III) reference IrCl$_3$ in Figure 4e. So we learn that Ir orbitals in IrBL-Red form

a well-defined σ-antibonding conduction state above the Fermi level and are in fully filled π-antibonding states below the Fermi level, plausibly being close to the Ir(III) oxidation state. The narrow excitation width reflects a narrow bandwidth of the 5d orbital in the IrBL.

Figure 5b presents the full E_i dependence spectra of IrO$_x$-Red. Like the case in the IrBL-Red, the maximum intensity is at around 3.2 eV, whose intensity is resonantly peaked resonates at around E_i = 11.216 keV. The excitation width is larger than that in IrBL. The apparent difference from the case in the IrBL-Red is that a finite scattering intensity is clearly visible in the low energy loss region below 2 eV, which resonates at around E_i = 11.215 keV. This low energy

scattering extends down to the zero energy loss like IrO$_2$, implying a metallic phase. These spectra suggest that Ir orbitals in the IrO$_x$-Red form a well-defined σ-antibonding conduction state above the Fermi level and have a small number of holes in the π-symmetry states.

To see all allowed excitations, the integrated RIXS spectrum is obtained by summing over all measured E_i dependence spectra. Figure 6a shows the Ir(IV) reference IrO$_2$ spectra. The low-energy region below 3 eV is denoted by A and consists of two peaks at around 0.5 and 2 eV. Two Gaussian functions fit two peaks. The high-energy region above 3 eV is denoted by B and consists of one broad asymmetric peak, which is fitted with two Gaussian functions. Figure 6b shows the 5d orbital density of states from density functional theory (DFT) calculations (details in the Supporting Information). The π-antibonding orbital states are mostly occupied and cross the Fermi level with one hole state. The absorption of 2p$^{3/2}$ to this one π hole state leads to the low-energy excitations in the A region. The 2 eV peak in Figure 6a can be associated with the high density of π-antibonding states at around −2 eV binding energy. In the DFT, the 2 eV binding energy states originate from the π orbitals that lie within the plane formed by the shared edges. The σ-antibonding orbital state is centered around 3 eV with its onset near 1 eV above the Fermi level. The absorption of 2p$^{3/2}$ to this σ conduction state leads to the high-energy excitations in the B region.

Figure 6c,d presents the integrated IrBL-Red and IrO$_x$-Red spectra, respectively. The high-energy excitations have noticeably smaller widths compared to the case in IrO$_2$, which reflect a smaller bandwidth of the 5d orbital in IrBL-Red and IrO$_x$-Red, which is understood as arising from a lack of translational periodicity of the nanostructure, the larger Ir−O bond length, and the lower-symmetry structural distortion. The high-energy excitations in IrBL-Red and IrO$_x$-Red are fitted with three Gaussian functions. The IrBL-Red spectrum in Figure 6c shows a negligible intensity below 1.5 eV, indicating its insulting electric property. The IrO$_x$-Red spectrum in Figure 6d shows rather a broad low-energy excitation, which is fitted with one broad Gaussian function. Table 2 summarizes fit results in terms of energy, width, and total intensity. Regarding the high-energy peak, the IrO$_x$ consists of peaks with larger widths than the IrBL-Red, suggesting a larger 5d bandwidth in the IrO$_x$-Red than in the IrBL-Red. The low-energy peak of IrO$_x$ has the full width at half-maximum (FWHM) of 1.82 eV, indicating a wide width π-antibonding state, which cannot be

gapped by the moderate Coulomb repulsion of the 5d orbital and explains the metallic electric property in the IrO$_x$-Red.

In Table 2, we calculate the total low-energy peak intensity divided by the total high-energy peak intensity (denoted by IR) for IrO$_2$ and IrO$_x$-Red. The IR values of IrO$_2$ and IrO$_x$-Red are 0.255 and 0.133, respectively. This IR value is proportional to the ratio of the π-state hole number and the σ-state hole number in the first approximation and so is closely related to the Ir valency. For example, one π-state hole and four σ-state hole of the Ir(IV) valency in IrO$_2$ produce IR = 1/4 = 0.25. Considering a resonance prefactor in the RIXS spectrum, an overlap of the low- and high-energy excitations, and orbital relaxations, it seems to be accidental that the experimental IR value of IrO$_2$ is very close to the nominal value of 0.25. However, even with this limitation, it can be safely stated that the IrO$_x$-Red has a mixed Ir valency between Ir(III) and Ir(IV).

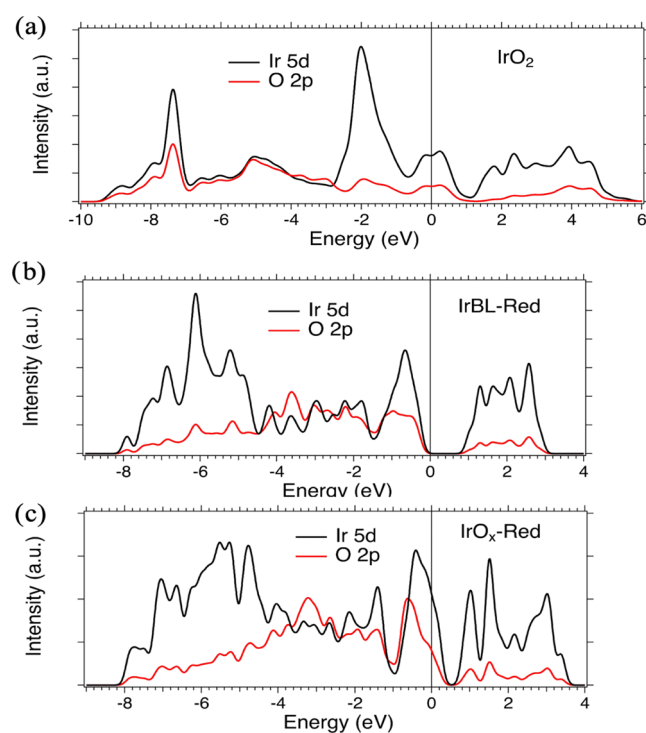**Band Structures of IrBL-Red and IrO$_x$-Red.** Figure 7a shows density functional theory calculations of the 5d and O

Figure 7. Band structure calculations for (a) the rutile crystalline IrO$_2$, (b) IrBL-Red, and (c) IrO$_x$-Red. The nanostructures refined by the PDF measurements and analyses were used for the calculations of the IrBL-Red and IrO$_x$-Red. The Fermi levels in two OECs were assumed based on the RIXS measurements.

Table 2. Summary of Fit Results[a]

		low-energy peaks		high-energy peaks		IR
IrO$_2$	energy	0.51	1.99	3.63	5.10	0.255
	width	1.04	1.21	1.75	2.43	
	int.	185	676	1833	1544	
IrBL-Red	energy			2.54	3.35	4.00
	width			0.71	1.02	2.52
	int.			373	984	949
IrO$_x$-Red	energy	1.20	2.28	3.16	4.0	0.133
	width	1.82	1.00	1.41	2.52	
	int.	350	338	1264	1025	

[a]Energy is the energy loss, and width is the full width at half-maximum (FWHM) of Gaussian fit peak. Units of energy and width are eV. Int. means the total intensity of the peak. IR is the total low-energy peak intensity divided by the total high-energy peak intensity.

2p partial density of states for the rutile IrO$_2$.[36] The σ-bonding, π-bonding, π-antibonding, and σ-antibonding states are located at around −8, −5, −2, and 3 eV, respectively. The occupied valence state has as large as 10 eV bandwidth. The π- and σ-antibonding states are responsible for the metallic carriers and the unoccupied conduction state, respectively. The fact that the RIXS excitations in IrO$_2$ are well defined within the 7 eV energy window as shown in Figure 6a suggests that these π- and σ-antibonding states mainly contribute to the RIXS excitations. Higher-binding-energy states do not contribute to well-defined electron−hole excitons but possibly fluorescence-like continuum scatterings at higher energies.

The DFT calculations were carried out for IrBL-Red and IrO$_x$-Red. Like the way of constructing the nanostructures in Figure 3, we assumed Ir-oxo vacants rutile structures (details in the Supporting Information). Here, we note that these DFT calculations based on the long-ranged structures have clear limitations of correspondence to the real electronic structures of the nanostructured IrBL and IrO$_x$. However, it is useful to study the effects of the longer Ir−O bond lengths, the smaller/larger Ir−O−Ir bond angles, and the lower-symmetry structural distortions in IrBL-Red and IrO$_x$-Red on the electronic structure.

Figure 7b,c shows the 5d and O 2p partial density of states for IrBL-Red and IrO$_x$-Red, respectively. The σ-bonding states at around −6 eV show large (small) Ir 5d (O 2p) density of states. A similar σ-bonding state feature was also seen in Ir vacant iridium oxides (Ir$_{47}$O$_{96}$ and Ir$_3$O$_8$).[15] Here, we pay attention to the antibonding state which mainly contributes to the RIXS excitations as learned from the case of IrO$_2$. The σ-antibonding states are located at around 2 eV above the Fermi level for both cases. Interestingly, the gap between the π-antibonding and the σ-antibonding states is large in the case of IrBL-Red but small in the case of IrO$_x$-Red due to the different bandwidth of the σ-antibonding state. In the case of IrBL-Red, the Fermi level can be drawn at the top of the π-antibonding state to describe the absence of low-energy excitation and the large gap in the RIXS spectrum of IrBL-Red (Figures 5a and 7b). In the case of IrO$_x$-Red, the Fermi level can be drawn at around 0.5 eV below the top of the π-antibonding state to describe the low-energy excitations in the RIXS spectra (Figures 5b and 7c). As seen in the case of IrO$_2$, the interband transitions between the π-antibonding and the σ-antibonding states give rise to the high-energy excitation around 3 eV. The bandwidth of the σ-antibonding state is larger in IrO$_x$-Red than IrBL-Red which is consistent with the observation that the width of the high-energy excitation is larger in IrO$_x$-Red than IrBL-Red.

■ DISCUSSION

Atomic Structure and Electronic State. The PDF measurement and analysis in this study show that atomic structures of IrBL-Red and IrO$_x$-Red are properly described as consisting of three edge-sharing and two corner-sharing octahedra. The Ir−O bond length is larger in IrBL-Red than IrO$_x$-Red while the edge- and corner-sharing bond angles are larger in IrO$_x$-Red than IrBL-Red as seen in Table 1. Local octahedral distortions which lead to the lower site symmetries are overall larger in IrO$_x$-Red than IrBL-Red. These structural differences have effects on Ir 5d orbital overlap, degeneracy, bandwidth, and crystal-field splitting, which are expected to influence the redox and OER catalytic properties.

Detailed electronic structure information of IrBL-Red and IrO$_x$-Red is provided by the RIXS measurements and the band structure calculations. The band structure calculations show that the large crystal fields and orbital overlaps of Ir 5d orbitals of IrBL-Red and IrO$_x$-Red give rise to σ-antibonding conduction states above the Fermi level and π-antibonding valence states around the Fermi level as found in the rutile IrO$_2$.[36] The bandwidths of the σ- and π-antibonding states are narrower in IrBL-Red than IrO$_x$-Red where the longer Ir−O bond length and smaller bond angles of IrBL-Red play key roles in reducing the bandwidth. The high-energy peaks at around 3 eV in the RIXS spectra of IrBL-Red and IrO$_x$-Red are associated with the interband transition between the π- and σ-

antibonding states. Smaller bandwidths of IrBL-Red result in the narrower excitation widths of the high-energy feature in IrBL-Red than that in IrO$_x$-Red.

The salient feature in the RIXS spectra of IrBL-Red is that there is negligible intensity below 2 eV, as seen in Figures 5a and 7b. The smaller bandwidth of the σ-antibonding state in IrBL-Red largely contributes to the large energy gap between π- and σ-antibonding as seen in the RIXS spectrum and band structure calculations. This spectral feature resembles that of the Ir(III)Cl$_3$ reference in Figure 4e. This suggests that Ir ions in IrBL-Red have the fully filled π-antibonding states and the integer filling of the Ir 5d orbitals, plausibly pointing to the Ir(III) oxidation state in IrBL-Red. Therefore, the RIXS measurement provides an effective way of identifying the integer filling state of the Ir 5d orbitals such as the Ir(III) oxidation state. Note that special care should be taken to use the XAS analysis for the estimation of the oxidation state because the XAS white line energy is a function of many factors such as the crystal-field splitting, the hybridization, and the bandwidth besides the Ir oxidation state.

In a noninteger filling case of the Ir 5d orbitals, the oxidation state estimation is subtle in the RIXS measurement. The RIXS spectra of IrO$_x$-Red show a finite scattering intensity in the low energy loss region below 2 eV, indicating that Ir ions in IrO$_x$-Red have noninteger filling of the Ir 5d orbitals. We estimate the ratio between low energy intensity and high energy intensity which is proportional to the ratio of the π-state hole number and the σ-state hole number in the first approximation and conclude that IrO$_x$-Red has a higher Ir oxidation state than IrBL-Red but a lower Ir oxidation state than IrO$_2$, and possibly has a mixed Ir valency between Ir(III) and Ir(IV). Note that the literature values of the Ir oxidation state in IrO$_x$ are quite scattered, ranging between 2.5+ and 6+ (see Figure S15).[15,19,22,24,39,40] The relation between the Ir−O bond length and the Ir oxidation state was reported to have the tendency that a shorter Ir−O bond length goes with a higher Ir oxidation state (or higher Ir hole number).[15] The lower Ir oxidation states found in the RIXS measurements of IrBL-Red and IrO$_x$-Red are consistent with this tendency.

Electrocatalytic Properties and Electronic Structure in the Reduction Condition. In the electrocatalytic properties, there are many other factors than electronic states such as surface functional groups which is beyond the scope of this work. Here, having verified different electronic structures in IrBL-Red and IrO$_x$-Red depending on different nanostructures, our discussion is focused on the relationship of electrocatalytic properties with electronic states of IrBL-Red and IrO$_x$-Red. Before going on, we note that the RIXS and PDF measurements in this work probe bulk electronic and atomic structures. Therefore, electronic and atomic structures of the surface are assumed to be the same as those of the bulk.

The pre-features in Figure 1a indicate that IrBL has a much larger overpotential than IrO$_x$ which is attributed to a poor electric conductivity in IrBL. In this work, we show that IrBL has the insulating electronic structure in the reduction condition. It can be assumed that the surface states are altered from the reduction condition, but the bulk state retains the insulating sites of the reduction state. Then, the poor electric conductivity in IrBL can be understood. The surface morphology data in Figure S1b,f show that IrBL-Red has a larger grain size than IrO$_x$-Red. Smaller surface area but the bigger bulk volume of larger grains can contribute to the poor electric conductivity in IrBL. In the case of IrO$_x$, the metallic

electronic structure is observed in the reduction condition, which can lead to good conductivity and small overpotential.

Reliable comparison of the OER activity requires detailed studies on active surface sites and area, which are not trivial in amorphous catalysts and are not attempted in this study. Here, the Ir contents of IrBL-Red and IrO_x-Red films were measured by the ICP measurement and used to normalize the CV data.[41,42] Figure 1b shows that IrBL has much lower OER activity than IrO_x. The larger voltage of pre-features and the larger overpotential of IrBL, as mentioned before, indicate an insulating behavior, and seem to be correlated with the lower OER activity of IrBL. In this sense, it can be speculated that the insulating electronic structure in the reduction condition of IrBL can be thought as detrimental for the OER activity and the metallic electronic structure in the reduction condition of IrO_x gives rise to a better OER activity. Electronic and atomic structures at higher potentials can be different from those in the reduction state. So, it will be interesting and important to monitor the evolution of the electronic and atomic structure by *in situ/operando* studies.

CONCLUSIONS

In this work, two iridium oxide catalysts in their reduction conditions have been studied by the PDF and RIXS techniques. The atomic structure model constructed by extracting Ir-oxo fragments from the rutile IrO_2 structure reasonably describes the PDF spectra of IrBL-Red and IrO_x-Red. Ir ions in IrBL-Red and IrO_x-Red have longer Ir−O bond lengths and smaller edge- and larger corner-sharing bond angles than the rutile IrO_2 and trigonal-type octahedral distortions. We show that antibonding states near the Fermi level mainly contribute to well-defined electron−hole excitons in the RIXS spectra of Ir compounds. The interband transitions between π- and σ-antibonding states show up as the main excitations in IrBL-Red and IrO_x-Red, which are located similarly at around 3 eV in both IrBL and IrO_x. The drastic difference in IrBL-Red and IrO_x-Red is found in the low-energy excitations which originate from the π-antibonding states. IrBL-Red is the large charge gap insulator with the integer filling of the Ir 5d orbitals while IrO_x-Red is metallic with the noninteger filling of the Ir 5d orbitals. Effects of the bond lengths and angles and the lower-symmetry structural distortions in IrBL-Red and IrO_x-Red on the electronic structure are investigated by band structure calculations assuming the refined atomic structures, which are found to be consistent with the experimental observations from the RIXS spectra. The large crystal fields and orbital overlaps of Ir 5d orbitals in IrBL-Red and IrO_x-Red play a key role in determining the Ir 5d orbital states in IrBL-Red and IrO_x-Red and structural details lead to marked differences in the Ir 5d orbital states between IrBL-Red and IrO_x-Red. We propose that different electronic and atomic structures in the reduction condition of IrBL and IrO_x provide different OER activity. Given that RIXS at the L_3 edge provides valuable information of the Ir 5d orbital states of *ex situ* OECs, an *in situ/operando* RIXS and PDF study is an interesting and vital effort to see the evolution of the electronic and atomic structures at high potentials and understand charge transfer energetics and kinetics of the OER under true conditions.

ASSOCIATED CONTENT

ⓈI Supporting Information

The Supporting Information is available free of charge at https://pubs.acs.org/doi/10.1021/acscatal.1c00818.

Experimental details (PDF)

AUTHOR INFORMATION

Corresponding Authors

Gihan Kwon − *National Synchrotron Light Source II, Brookhaven National Laboratory, Upton, New York 11973, United States;* ⓘ orcid.org/0000-0002-7963-2136; Email: gkwon@bnl.gov

Seo Hyoung Chang − *Department of Physics, Chung-Ang University, Seoul 06974, Republic of Korea;* ⓘ orcid.org/0000-0002-1012-7983; Email: cshyoung@cau.ac.kr

Jungho Kim − *X-Ray Science Division, Advanced Photon Source, Argonne National Laboratory, Lemont, Illinois 60439, United States;* ⓘ orcid.org/0000-0003-4560-6375; Email: jhkim@anl.gov

Authors

Jin Eun Heo − *Department of Physics, Chung-Ang University, Seoul 06974, Republic of Korea*

Kyeong Jun Lee − *Department of Physics, Chung-Ang University, Seoul 06974, Republic of Korea*

Jin-Kwang Kim − *Department of Physics, Pohang University of Science and Technology, Pohang, Gyeongbuk 37673, Republic of Korea; Center for Artificial Low Dimensional Electronic Systems, Institute for Basic Science (IBS), Pohang, Gyeongbuk 37673, Republic of Korea*

Byeong-Gwan Cho − *Pohang Accelerator Laboratory, Pohang, Gyeongbuk 37673, Republic of Korea*

Tae Yeong Koo − *Pohang Accelerator Laboratory, Pohang, Gyeongbuk 37673, Republic of Korea*

B. J. Kim − *Department of Physics, Pohang University of Science and Technology, Pohang, Gyeongbuk 37673, Republic of Korea; Center for Artificial Low Dimensional Electronic Systems, Institute for Basic Science (IBS), Pohang, Gyeongbuk 37673, Republic of Korea*

Chanseok Kim − *School of Energy and Chemical Engineering, Ulsan National Institute of Science and Technology (UNIST), Ulsan 44919, Republic of Korea*

Jun Hee Lee − *School of Energy and Chemical Engineering, Ulsan National Institute of Science and Technology (UNIST), Ulsan 44919, Republic of Korea;* ⓘ orcid.org/0000-0001-5121-244X

Seong-Min Bak − *National Synchrotron Light Source II, Brookhaven National Laboratory, Upton, New York 11973, United States;* ⓘ orcid.org/0000-0002-1626-5949

Kevin A. Beyer − *X-Ray Science Division, Advanced Photon Source, Argonne National Laboratory, Lemont, Illinois 60439, United States*

Hui Zhong − *Joint Photon Sciences Institute, Stony Brook University, Stony Brook, New York 11794, United States*

Robert J. Koch − *Condensed Matter Physics and Materials Science Department, Brookhaven National Laboratory, Upton, New York 11973, United States;* ⓘ orcid.org/0000-0003-4995-2101

Sooyeon Hwang − *Center for Functional Nanomaterials, Brookhaven National Laboratory, Upton, New York 11973, United States;* ⓘ orcid.org/0000-0001-5606-6728

Lisa M. Utschig − *Chemical Sciences and Engineering Division, Argonne National Laboratory, Lemont, Illinois 60439, United States;* orcid.org/0000-0003-2095-5392

Xiaojing Huang − *National Synchrotron Light Source II, Brookhaven National Laboratory, Upton, New York 11973, United States*

Gongfang Hu − *Department of Chemistry, Yale University, New Haven, Connecticut 06520, United States;* orcid.org/0000-0002-0387-9079

Gary W. Brudvig − *Department of Chemistry, Yale University, New Haven, Connecticut 06520, United States;* orcid.org/0000-0002-7040-1892

David M. Tiede − *Chemical Sciences and Engineering Division, Argonne National Laboratory, Lemont, Illinois 60439, United States;* orcid.org/0000-0002-2784-4954

Complete contact information is available at:
https://pubs.acs.org/10.1021/acscatal.1c00818

Notes
The authors declare no competing financial interest.

ACKNOWLEDGMENTS

REFERENCES

(1) Spöri, C.; Kwan, J. T. H.; Bonakdarpour, A.; Wilkinson, D. P.; Strasser, P. The Stability Challenges of Oxygen Evolving Catalysts: Towards a Common Fundamental Understanding and Mitigation of Catalyst Degradation. *Angew. Chem., Int. Ed.* **2017**, *56*, 5994−6021.

(2) Nong, H. N.; Gan, L.; Willinger, E.; Teschner, D.; Strasser, P. IrOx core-shell nanocatalysts for cost- and energy-efficient electrochemical water splitting. *Chem. Sci.* **2014**, *5*, 2955−2963.

(3) Reier, T.; Pawolek, Z.; Cherevko, S.; Bruns, M.; Jones, T.; Teschner, D.; Selve, S.; Bergmann, A.; Nong, H. N.; Schlögl, R.; Mayrhofer, K. J. J.; Strasser, P. Molecular Insight in Structure and Activity of Highly Efficient, Low-Ir Ir−Ni Oxide Catalysts for Electrochemical Water Splitting (OER). *J. Am. Chem. Soc.* **2015**, *137*, 13031−13040.

(4) Oh, H.-S.; Nong, H. N.; Reier, T.; Bergmann, A.; Gliech, M.; Ferreira de Araújo, J.; Willinger, E.; Schlögl, R.; Teschner, D.; Strasser, P. Electrochemical Catalyst−Support Effects and Their Stabilizing Role for IrOx Nanoparticle Catalysts during the Oxygen Evolution Reaction. *J. Am. Chem. Soc.* **2016**, *138*, 12552−12563.

(5) Esquius, J. R.; Algara-Siller, G.; Spanos, I.; Freakley, S. J.; Schlögl, R.; Hutchings, G. J. Preparation of Solid Solution and Layered IrOx−Ni(OH)$_2$ Oxygen Evolution Catalysts: Toward Optimizing Iridium Efficiency for OER. *ACS Catal.* **2020**, *10*, 14640−14648.

(6) Lim, J.; Yang, S.; Kim, C.; Roh, C.-W.; Kwon, Y.; Kim, Y.-T.; Lee, H. Shaped Ir−Ni bimetallic nanoparticles for minimizing Ir utilization in oxygen evolution reaction. *Chem. Commun.* **2016**, *52*, 5641−5644.

(7) McCrory, C. C. L.; Jung, S.; Ferrer, I. M.; Chatman, S. M.; Peters, J. C.; Jaramillo, T. F. Benchmarking Hydrogen Evolving Reaction and Oxygen Evolving Reaction Electrocatalysts for Solar Water Splitting Devices. *J. Am. Chem. Soc.* **2015**, *137*, 4347−4357.

(8) Danilovic, N.; Subbaraman, R.; Chang, K.-C.; Chang, S. H.; Kang, Y. J.; Snyder, J.; Paulikas, A. P.; Strmcnik, D.; Kim, Y.-T.; Myers, D.; Stamenkovic, V. R.; Markovic, N. M. Activity−Stability Trends for the Oxygen Evolution Reaction on Monometallic Oxides in Acidic Environments. *J. Phys. Chem. Lett.* **2014**, *5*, 2474−2478.

(9) Blakemore, J. D.; Schley, N. D.; Olack, G. W.; Incarvito, C. D.; Brudvig, G. W.; Crabtree, R. H. Anodic deposition of a robust iridium-based water-oxidation catalyst from organometallic precursors. *Chem. Sci.* **2011**, *2*, 94−98.

(10) Blakemore, J. D.; Schley, N. D.; Kushner-Lenhoff, M. N.; Winter, A. M.; D'Souza, F.; Crabtree, R. H.; Brudvig, G. W. Comparison of Amorphous Iridium Water-Oxidation Electrocatalysts Prepared from Soluble Precursors. *Inorg. Chem.* **2012**, *51*, 7749−7763.

(11) Irshad, A.; Munichandraiah, N. High Catalytic Activity of Amorphous Ir-Pi for Oxygen Evolution Reaction. *ACS Appl. Mater. Interfaces* **2015**, *7*, 15765−15776.

(12) Smith, R. D. L.; Sporinova, B.; Fagan, R. D.; Trudel, S.; Berlinguette, C. P. Facile Photochemical Preparation of Amorphous Iridium Oxide Films for Water Oxidation Catalysis. *Chem. Mater.* **2014**, *26*, 1654−1659.

(13) Reier, T.; Oezaslan, M.; Strasser, P. Electrocatalytic Oxygen Evolution Reaction (OER) on Ru, Ir, and Pt Catalysts: A Comparative Study of Nanoparticles and Bulk Materials. *ACS Catal.* **2012**, *2*, 1765−1772.

(14) Reier, T.; Teschner, D.; Lunkenbein, T.; Bergmann, A.; Selve, S.; Kraehnert, R.; Schlögl, R.; Strasser, P. Electrocatalytic Oxygen Evolution on Iridium Oxide: Uncovering Catalyst-Substrate Interactions and Active Iridium Oxide Species. *J. Electrochem. Soc.* **2014**, *161*, F876−F882.

(15) Nong, H. N.; Reier, T.; Oh, H.-S.; Gliech, M.; Paciok, P.; Vu, T. H. T.; Teschner, D.; Heggen, M.; Petkov, V.; Schlögl, R.; Jones, T.; Strasser, P. A unique oxygen ligand environment facilitates water oxidation in hole-doped IrNiOx core−shell electrocatalysts. *Nat. Catal.* **2018**, *1*, 841−851.

(16) Steegstra, P.; Busch, M.; Panas, I.; Ahlberg, E. Revisiting the Redox Properties of Hydrous Iridium Oxide Films in the Context of Oxygen Evolution. *J. Phys. Chem. C* **2013**, *117*, 20975−20981.

(17) Minguzzi, A.; Lugaresi, O.; Achilli, E.; Locatelli, C.; Vertova, A.; Ghigna, P.; Rondinini, S. Observing the oxidation state turnover in heterogeneous iridium-based water oxidation catalysts. *Chem. Sci.* **2014**, *5*, 3591−3597.

(18) Choy, J.-H.; Kim, D.-K.; Demazeau, G.; Jung, D.-Y. LIII-Edge XANES Study on Unusually High Valent Iridium in a Perovskite Lattice. *J. Phys. Chem. A* **1994**, *98*, 6258−6262.

(19) Choy, J.-H.; Kim, D.-K.; Hwang, S.-H.; Demazeau, G.; Jung, D.-Y. XANES and EXAFS Studies on the Ir-O Bond Covalency in Ionic Iridium Perovskites. *J. Am. Chem. Soc.* **1995**, *117*, 8557−8566.

(20) Minguzzi, A.; Locatelli, C.; Lugaresi, O.; Achilli, E.; Cappelletti, G.; Scavini, M.; Coduri, M.; Masala, P.; Sacchi, B.; Vertova, A.; Ghigna, P.; Rondinini, S. Easy Accommodation of Different Oxidation

States in Iridium Oxide Nanoparticles with Different Hydration Degree as Water Oxidation Electrocatalysts. *ACS Catal.* **2015**, *5*, 5104−5115.

(21) Li, L.; Yang, J.; Ali-Löytty, H.; Weng, T.-C.; Toma, F. M.; Sokaras, D.; Sharp, I. D.; Nilsson, A. Operando Observation of Chemical Transformations of Iridium Oxide During Photoelectrochemical Water Oxidation. *ACS Appl. Energy Mater.* **2019**, *2*, 1371−1379.

(22) Mo, Y.; Stefan, I. C.; Cai, W.-B.; Dong, J.; Carey, P.; Scherson, D. A. In Situ Iridium LIII-Edge X-ray Absorption and Surface Enhanced Raman Spectroscopy of Electrodeposited Iridium Oxide Films in Aqueous Electrolytes. *J. Phys. Chem. B* **2002**, *106*, 3681−3686.

(23) Zhao, Y.; Vargas-Barbosa, N. M.; Hernandez-Pagan, E. A.; Mallouk, T. E. Anodic Deposition of Colloidal Iridium Oxide Thin Films from Hexahydroxyiridate(IV) Solutions. *Small* **2011**, *7*, 2087−2093.

(24) Hüppauff, M.; Lengeler, B. Valency and Structure of Iridium in Anodic Iridium Oxide Films. *J. Electrochem. Soc.* **1993**, *140*, 598−602.

(25) Pedersen, A. F.; Escudero-Escribano, M.; Sebok, B.; Bodin, A.; Paoli, E.; Frydendal, R.; Friebel, D.; Stephens, I. E. L.; Rossmeisl, J.; Chorkendorff, I.; Nilsson, A. Operando XAS Study of the Surface Oxidation State on a Monolayer IrOx on RuOx and Ru Oxide Based Nanoparticles for Oxygen Evolution in Acidic Media. *J. Phys. Chem. B* **2018**, *122*, 878−887.

(26) Casalongue, H. G. S.; Ng, M. L.; Kaya, S.; Friebel, D.; Ogasawara, H.; Nilsson, A. In Situ Observation of Surface Species on Iridium Oxide Nanoparticles during the Oxygen Evolution Reaction. *Angew. Chem., Int. Ed.* **2014**, *53*, 7169−7172.

(27) Imada, M.; Fujimori, A.; Tokura, Y. Metal-insulator transitions. *Rev. Mod. Phys.* **1998**, *70*, 1039−1263.

(28) Kim, B. J.; Jin, H.; Moon, S. J.; Kim, J. Y.; Park, B. G.; Leem, C. S.; Yu, J.; Noh, T. W.; Kim, C.; Oh, S. J.; Park, J. H.; Durairaj, V.; Cao, G.; Rotenberg, E. Novel J_{eff} = 1/2 Mott State Induced by Relativistic Spin-Orbit Coupling in Sr$_2$IrO$_4$. *Phys. Rev. Lett.* **2008**, *101*, No. 076402.

(29) Huang, J.; Blakemore, J. D.; Fazi, D.; Kokhan, O.; Schley, N. D.; Crabtree, R. H.; Brudvig, G. W.; Tiede, D. M. Domain structure for an amorphous iridium-oxide water-oxidation catalyst characterized by X-ray pair distribution function analysis. *Phys. Chem. Chem. Phys.* **2014**, *16*, 1814−1819.

(30) Willinger, E.; Massué, C.; Schlögl, R.; Willinger, M. G. Identifying Key Structural Features of IrOx Water Splitting Catalysts. *J. Am. Chem. Soc.* **2017**, *139*, 12093−12101.

(31) Blakemore, J. D.; Mara, M. W.; Kushner-Lenhoff, M. N.; Schley, N. D.; Konezny, S. J.; Rivalta, I.; Negre, C. F. A.; Snoeberger, R. C.; Kokhan, O.; Huang, J.; Stickrath, A.; Tran, L. A.; Parr, M. L.; Chen, L. X.; Tiede, D. M.; Batista, V. S.; Crabtree, R. H.; Brudvig, G. W. Characterization of an Amorphous Iridium Water-Oxidation Catalyst Electrodeposited from Organometallic Precursors. *Inorg. Chem.* **2013**, *52*, 1860−1871.

(32) Kim, J.; Casa, D.; Upton, M. H.; Gog, T.; Kim, Y.-J.; Mitchell, J. F.; van Veenendaal, M.; Daghofer, M.; van den Brink, J.; Khaliullin, G.; Kim, B. J. Magnetic Excitation Spectra of Sr$_2$IrO$_4$ Probed by Resonant Inelastic X-Ray Scattering: Establishing Links to Cuprate Superconductors. *Phys. Rev. Lett.* **2012**, *108*, No. 177003.

(33) Du, P.; Kokhan, O.; Chapman, K. W.; Chupas, P. J.; Tiede, D. M. Elucidating the Domain Structure of the Cobalt Oxide Water Splitting Catalyst by X-ray Pair Distribution Function Analysis. *J. Am. Chem. Soc.* **2012**, *134*, 11096−11099.

(34) Jayashree, S.; Ashokkumar, M. Switchable Intrinsic Defect Chemistry of Titania for Catalytic Applications. *Catalysts* **2018**, *8*, No. 601.

(35) Mattheiss, L. F. Electronic structure of RuO$_2$, OsO$_2$, and IrO$_2$. *Phys. Rev. B* **1976**, *13*, 2433−2450.

(36) Kahk, J. M.; Poll, C. G.; Oropeza, F. E.; Ablett, J. M.; Céolin, D.; Rueff, J. P.; Agrestini, S.; Utsumi, Y.; Tsuei, K. D.; Liao, Y. F.; Borgatti, F.; Panaccione, G.; Regoutz, A.; Egdell, R. G.; Morgan, B. J.; Scanlon, D. O.; Payne, D. J. Understanding the Electronic Structure of IrO$_2$ Using Hard-X-ray Photoelectron Spectroscopy and Density-Functional Theory. *Phys. Rev. Lett.* **2014**, *112*, No. 117601.

(37) Shvyd'ko, Y. V.; Hill, J. P.; Burns, C. A.; Coburn, D. S.; Brajuskovic, B.; Casa, D.; Goetze, K.; Gog, T.; Khachatryan, R.; Kim, J. H.; Kodituwakku, C. N.; Ramanathan, M.; Roberts, T.; Said, A.; Sinn, H.; Shu, D.; Stoupin, S.; Upton, M.; Wieczorek, M.; Yavas, H. MERIX—Next generation medium energy resolution inelastic X-ray scattering instrument at the APS. *J. Electron Spectrosc. Relat. Phenom.* **2013**, *188*, 140−149.

(38) Gog, T.; Casa, D. M.; Said, A. H.; Upton, M. H.; Kim, J.; Kuzmenko, I.; Huang, X.; Khachatryan, R. Spherical analyzers and monochromators for resonant inelastic hard X-ray scattering: a compilation of crystals and reflections. *J. Synchrotron Radiat.* **2013**, *20*, 74−79.

(39) Hillman, A. R.; Skopek, M. A.; Gurman, S. J. X-Ray spectroscopy of electrochemically deposited iridium oxide films: detection of multiple sites through structural disorder. *Phys. Chem. Chem. Phys.* **2011**, *13*, 5252−5263.

(40) Achilli, E.; Minguzzi, A.; Lugaresi, O.; Locatelli, C.; Rondinini, S.; Spinolo, G.; Ghigna, P. In Situ Dispersive EXAFS in Electrocatalysis: The Investigation of the Local Structure of IrOx in Chronoamperometric Conditions as a Case Study. *J. Spectrosc.* **2014**, *2014*, No. 480102.

(41) Kim, Y.-T.; Lopes, P. P.; Park, S.-A.; Lee, A. Y.; Lim, J.; Lee, H.; Back, S.; Jung, Y.; Danilovic, N.; Stamenkovic, V.; Erlebacher, J.; Snyder, J.; Markovic, N. M. Balancing activity, stability and conductivity of nanoporous core-shell iridium/iridium oxide oxygen evolution catalysts. *Nat. Commun.* **2017**, *8*, No. 1449.

(42) Zhao, S.; Yu, H.; Maric, R.; Danilovic, N.; Capuano, C. B.; Ayers, K. E.; Mustain, W. E. Calculating the Electrochemically Active Surface Area of Iridium Oxide in Operating Proton Exchange Membrane Electrolyzers. *J. Electrochem. Soc.* **2015**, *162*, F1292−F1298.